Aerospace Science and Technology 95 (2019) 105513

Contents lists available at ScienceDirect

Aerospace Science and Technology

www.elsevier.com/locate/aescte

A real-time hybrid aeroelastic simulation platform for flexible wings

Weihua Su [a,*], Wei Song [b]

[a] Department of Aerospace Engineering and Mechanics, The University of Alabama, Tuscaloosa, AL 35487-0280, United States
[b] Department of Civil, Construction and Environmental Engineering, The University of Alabama, Tuscaloosa, AL 35487-0205, United States

ARTICLE INFO

Article history:
Received 22 July 2019
Received in revised form 16 August 2019
Accepted 24 October 2019
Available online 25 October 2019

Keywords:
Hybrid simulation
Real-time
Aeroelastic behavior
Flexible wing

ABSTRACT

The concept of real-time hybrid aeroelastic simulation for flexible wings is introduced in this paper. In a hybrid aeroelastic simulation, a coupled aeroelastic system is "broken down" into an aerodynamic simulation subsystem and a structural vibration subsystem. The coupling between structural dynamics and aerodynamics is maintained by the real-time communication between the two subsystems. As the vibration of the testing article (a wing member or a full aircraft) is actuated by actuators, hybrid aeroelastic simulation and experiment can eliminate the sizing constraint of the conventional aeroelastic testing performed within a wind-tunnel. It also significantly saves the cost of wind-tunnel testing. However, several critical technical problems (such as process noise, measurement noise, and actuator delay) need to be addressed to enable a hybrid simulation in real-time. This paper proves the concept of real-time hybrid simulation and discusses some of the critical problems underlying the technique.

1. Introduction

In aeronautical engineering, both computational and experimental techniques are applied to understand the structural, aerodynamic, aeroelastic, and control characteristics of an aircraft wing member or the complete vehicle. There are millions of computational and experimental studies in aeronautical engineering, focusing on different types of wing and aircraft configurations under different flow and flight conditions. Direct experimental measurement of wing and aircraft responses from wind-tunnel testing is valuable and helpful to support the aircraft design. However, there are some situations where wind-tunnel experiments become inconvenient. For example, not all wind-tunnels can accommodate the modern large transport aircraft (e.g., Boeing 747 and Airbus 380) – this sizing constraint is especially significant for the wind-tunnels in universities for research purpose. Additionally, the energy and power constraint of most wind-tunnels limits people to study full-size supersonic and hypersonic vehicles experimentally. Even though experiments can be carried out with scaled models in wind-tunnels, they do not produce the exact data of full-size models' behaviors due to the mismatch in both structures and flow conditions.

On the other hand, numerical simulations become the most convenient approach to predict wing and aircraft responses. There are beam-, plate-, and shell-based finite-element models to represent different types of aircraft structures, which can be coupled with an appropriate aerodynamic model, such as the simple potential flow-based formulations or the sophisticated high-fidelity CFD tools. The accuracy of these aeroelastic formulations generally relies on the fidelity of both structural and aerodynamic models, as well as the coupling scheme involved in the simulation.

Alternatively, new investigation approaches are developed, where functional and self-contained hardware is designed in a computational simulation system to solve real problems. This approach is generally referred to as hardware-in-the-loop (HIL). Wei et al. [1] developed a hybrid simulation with the integration of celestial navigation hardware for satellite navigation. Waszniowski et al. [2] used a HIL simulation to correct the error pertained in their aircraft yaw control software. The approach was found to be efficient in error detection and isolation. Other studies in aerospace engineering that involve HIL can be found in the literature, including optimization of a morphing wing mechanism with wind tunnel hardware in the loop [3], testing of aircraft powerplant fuel cell with HIL [4], projectile control in a wind tunnel [5], control of a spacecraft [6], and verification of a small satellite's onboard software [7]. It can be seen that hybrid simulation systems have been successfully used as the testbed for verifying aircraft or spacecraft control algorithms and hardware implementations. However, in these studies, the data communication between software and hardware was usually one-way, i.e., the numerical component in these HIL simulation systems is not coupled with the experimental component. While this treatment is acceptable in several studies, this is in general not the

* Corresponding author.
E-mail address: suw@eng.ua.edu (W. Su).

https://doi.org/10.1016/j.ast.2019.105513
1270-9638/

Nomenclature

$\mathbf{A}$, $\mathbf{H}$ aeroelastic system matrices
$\mathbf{A}_1$, $\mathbf{B}_1$, $\mathbf{C}_1$, $\mathbf{D}_1$ system matrices of aerodynamic subsystem
$\mathbf{A}_2$, $\mathbf{B}_2$, $\mathbf{C}_2$, $\mathbf{D}_2$ system matrices of structural dynamic subsystem
b semichord of airfoil ..... m
$\bar{b}$ coefficients for inflow states
C_α damping coefficient in pitching ..... N s
C_ξ damping coefficient in plunging ..... N s m^{-2}
$\mathbf{D}_a$ aerodynamic sensitivity with respect to inflow states
d location of midchord point in front of elastic axis .. m
$\mathbf{E}$, $\mathbf{c}$, $\mathbf{F}_1$, $\mathbf{F}_2$, $\mathbf{F}_3$ coefficient matrices of inflow differential equations
f_1, f_2 actuator forces ..... N
g gravitational acceleration ..... m s^{-2}
I_α airfoil mass moment of inertia ..... kg m
K_α torsional spring constant per unit span ..... N
K_ξ linear spring constant per unit span ..... N m^{-2}
$\mathcal{L}$, $\mathcal{M}$ aerodynamic lift and moment on airfoil N m^{-1} and N
l_{01}, l_{02} initial actuator lengths ..... m
Δl_1, Δl_2 instantaneous actuator length changes ..... m
$\bar{\mathbf{M}}$, $\bar{\mathbf{C}}$, $\bar{\mathbf{K}}$ aeroelastic inertial, damping, and stiffness matrices
$\mathbf{M}_a$, $\mathbf{C}_a$, $\mathbf{K}_a$ aerodynamic inertial, damping, and stiffness matrices
$\mathbf{M}_s$, $\mathbf{C}_s$, $\mathbf{K}_s$ structural inertial, damping, and stiffness matrices
m airfoil mass ..... kg m^{-1}
N number of inflow states defined on airfoil
$\mathbf{q}$ vector of airfoil motion
$\mathbf{R}_0$ constant load vector
$\mathbf{R}$ aerodynamic load vector
r_1, r_2 arms of actuator forces from elastic axis ..... m
S_α airfoil structural imbalance ..... kg
s span of airfoil ..... m
U_0 free-stream velocity ..... m s^{-1}
$\mathbf{u}_1$, $\mathbf{x}_1$, $\mathbf{y}_1$ control input, state, and output of aerodynamic subsystem
$\mathbf{u}_2$, $\mathbf{x}_2$, $\mathbf{y}_2$ control input, state, and output of structural dynamic subsystem
$\mathbf{x}$ state of aeroelastic system
α rigid-body pitching of airfoil ..... rad
α_0 airfoil's initial pitching angle with unstretched torsional spring ..... rad
θ_1, θ_2 actuator orientations ..... rad
$\boldsymbol{\lambda}$ inflow states vector ..... m s^{-1}
λ_0 inflow velocity ..... m s^{-1}
ξ rigid-body plunging of airfoil ..... m
ρ air density ..... kg m^{-3}

case when studying flexible aircraft's aeroelasticity and flight dynamics in hybrid simulations, because the associated aeroelastic behavior of the flexible wings demands real-time interaction and coupling between the structural motion and the aerodynamic loads, which are, respectively, considered as numerical and experimental components in this study. Wallace et al. [8] conducted a hybrid simulation on the dynamics of a rotor blade and hub system. However, they focused on the nonlinear behavior of the dampers rather than the system's aeroelastic behavior, and cannot be applied to studying the aeroelastic response of flexible aircraft.

In addition to the coupling requirement in studying the aeroelastic response of flexible wings, it is also essential to obtain the real aerodynamic loads on the wings in real-time, to capture their accurate aeroelastic response. Therefore, this paper investigates a real-time hybrid simulation (RTHS) platform using the developed modeling and simulation techniques. Real-time hybrid simulation is an attractive alternative to complete dynamic structural model testing or simulation [9–11]. Real-time hybrid simulation is a novel, powerful, and cost-effective experimental technique for examining the behavior of complex, full-scale structural systems under realistic loading conditions. It originates from earthquake engineering as an attractive alternative to traditional shake table testing (Nakashima et al. [10]). Similar to the design in conventional hybrid simulation systems, the dynamic system under investigation is divided into experimental and numerical components in RTHS. The part that is less understood and/or difficult to model is built in the laboratory as the physical experiment component. However, the part that can be numerically simulated with good accuracy while being inconvenient and expensive to capture in experiments is considered as the numerical component. Necessary actuators and sensors are used to interface these two components to complete the hybrid simulation loop in real time. Because RTHS only requires to realize part of the structure physically – the experimental component, it significantly reduces the test requirements on both cost and space. This study proposes an RTHS platform to enable a promising experimental method to investigate large-scale wing and aircraft behavior and to verify robust and efficient control algorithms, under realistic loading conditions. To the best of the authors' knowledge, this is the first time an RTHS platform is proposed for studying the aeroelastic behaviors of flexible aircraft and wings.

2. Theoretical formulation

Instead of studying on a wing member or a full aircraft directly, this paper focuses on proving the concept of RTHS for a 2-D airfoil. Therefore, this section presents the aeroelastic formulation of a 2-D rigid airfoil, which is transformed into a state-space form for further development. The algorithm of RTHS and proof-of-concept study are then introduced.

2.1. 2-D airfoil section and unsteady aerodynamic loads

As shown in Fig. 1, the equation of motion of a thin airfoil section with plunging (ξ, positive down, measured from the position where the spring is balanced by the airfoil's weight) and pitching (α, positive nose up) degrees-of-freedom is given by

$$\begin{bmatrix} m & S_\alpha \\ S_\alpha & I_\alpha \end{bmatrix} \begin{Bmatrix} \ddot{\xi}(t) \\ \ddot{\alpha}(t) \end{Bmatrix} + \begin{bmatrix} C_\xi & 0 \\ 0 & C_\alpha \end{bmatrix} \begin{Bmatrix} \dot{\xi}(t) \\ \dot{\alpha}(t) \end{Bmatrix} + \begin{bmatrix} K_\xi & 0 \\ 0 & K_\alpha \end{bmatrix} \begin{Bmatrix} \xi(t) \\ \alpha(t) - \alpha_0 \end{Bmatrix} = \begin{Bmatrix} -\mathcal{L}(t) \\ \mathcal{M}(t) \end{Bmatrix} + \begin{Bmatrix} m \\ S_\alpha \end{Bmatrix} g \tag{1}$$

where m, S_α, and I_α are the total mass, structural imbalance, and mass moment of inertia of the airfoil, respectively, K_ξ and K_α are the linear and torsional spring constants per unit wingspan, respectively, C_ξ and C_α are the damping coefficients in plunging and pitching, respectively, and α_0 is the pitching angle when the torsional spring is not stretched. If one defines the degrees-of-freedom and system matrices as follows,

$$\mathbf{q}(t) = \begin{Bmatrix} \xi(t) \\ \alpha(t) \end{Bmatrix}, \quad \mathbf{M}_s = \begin{bmatrix} m & S_\alpha \\ S_\alpha & I_\alpha \end{bmatrix}, \quad \mathbf{C}_s = \begin{bmatrix} C_\xi & 0 \\ 0 & C_\alpha \end{bmatrix}, \quad \mathbf{K}_s = \begin{bmatrix} K_\xi & 0 \\ 0 & K_\alpha \end{bmatrix} \tag{2}$$

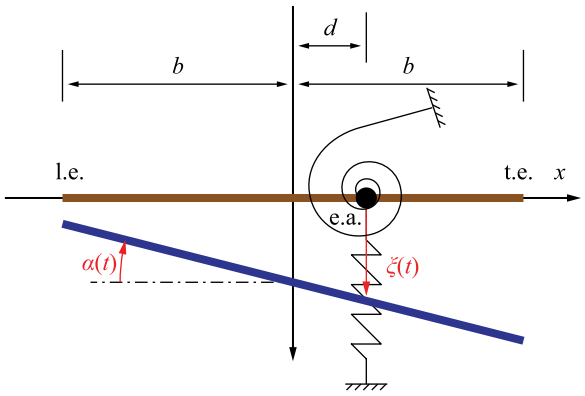

Fig. 1. A 2-D rigid airfoil section.

Eq. (1) can be simplified to

$$\mathbf{M}_s\ddot{\mathbf{q}}(t)+\mathbf{C}_s\dot{\mathbf{q}}(t)+\mathbf{K}_s\mathbf{q}(t)=\mathbf{R}(t)+\mathbf{R}_0 \tag{3}$$

with the load vectors being

$$\mathbf{R}(t)=\begin{Bmatrix}-\mathcal{L}(t)\\ \mathcal{M}(t)\end{Bmatrix},\quad \mathbf{R}_0=\begin{Bmatrix}0\\ K_\alpha\alpha_0\end{Bmatrix}+\begin{Bmatrix}m\\ S_\alpha\end{Bmatrix}g \tag{4}$$

where $\mathbf{R}(t)$ is the aerodynamic load, and $\mathbf{R}_0$ is a constant load due to the airfoil's non-zero initial pitching angle and its gravity.

The unsteady aerodynamic load $\mathbf{R}(t)$ at the elastic axis (e.a., where the two springs are attached to the airfoil) is calculated by using the finite-state inflow theory developed by Peters et al. [12–14]. The theory calculates aerodynamic loads on a thin airfoil section in incompressible, inviscid flow, given by

$$\begin{aligned}-\mathcal{L}&=-\pi\rho b^2\left(\ddot{\xi}+U_0\dot{\alpha}-d\ddot{\alpha}\right)\\&\quad-2\pi\rho bU_0^2\left[\alpha+\frac{\dot{\xi}}{U_0}+\left(\frac{1}{2}b-d\right)\frac{\dot{\alpha}}{U_0}-\frac{\lambda_0}{U_0}\right]\\ \mathcal{M}&=\pi\rho b^2\left[d\ddot{\xi}-\left(\frac{1}{2}b-d\right)U_0\dot{\alpha}-\left(\frac{1}{8}b^2+d^2\right)\ddot{\alpha}\right]\\&\quad+2\pi\rho bU_0^2\left(\frac{1}{2}b+d\right)\left[\alpha+\frac{\dot{\xi}}{U_0}+\left(\frac{1}{2}b-d\right)\frac{\dot{\alpha}}{U_0}-\frac{\lambda_0}{U_0}\right]\end{aligned} \tag{5}$$

where b is the semichord of the airfoil, d is the distance of the midchord in front of the elastic axis. The inflow parameter λ_0 accounts for induced flow due to the free vorticity, which is a weighted summation of the inflow states λ_i as described in Peters and Johnson [12], i.e.,

$$\lambda_0=\frac{1}{2}\sum_{i=1}^{N}\bar{b}_i\lambda_i \tag{6}$$

where N is the number of inflow states defined on the airfoil, and $\bar{b}$ are the coefficients that can be obtained by the least-square method [13]. Equation (5) can also be written in a compact form, given by

$$\mathbf{R}=\mathbf{M}_a\ddot{\mathbf{q}}+\mathbf{C}_a\dot{\mathbf{q}}+\mathbf{K}_a\mathbf{q}+\mathbf{D}_a\boldsymbol{\lambda} \tag{7}$$

where

$$\begin{aligned}\mathbf{M}_a&=\pi\rho b^2\begin{bmatrix}-1 & d\\ d & -\left(\frac{1}{8}b^2+d^2\right)\end{bmatrix},\\ \mathbf{C}_a&=2\pi\rho bU_0\begin{bmatrix}-1 & -(b-d)\\ \frac{1}{2}b+d & d\left(\frac{1}{2}b-d\right)\end{bmatrix},\\ \mathbf{K}_a&=2\pi\rho bU_0^2\begin{bmatrix}0 & -1\\ 0 & \frac{1}{2}b+d\end{bmatrix},\\ \mathbf{D}_a&=\pi\rho bU_0\begin{Bmatrix}1\\ -\left(\frac{1}{2}b+d\right)\end{Bmatrix}\begin{Bmatrix}\bar{b}_1 & \bar{b}_2 & \cdots & \bar{b}_N\end{Bmatrix}\end{aligned} \tag{8}$$

Finally, the governing equation for the inflow states is

$$\mathbf{E}\dot{\boldsymbol{\lambda}}+\frac{U_0}{b}\boldsymbol{\lambda}=\mathbf{c}\left[\ddot{\xi}+\left(\frac{1}{2}b-d\right)\ddot{\alpha}+U_0\dot{\alpha}\right] \tag{9}$$

where the coefficients $\mathbf{E}$ and $\mathbf{c}$ are both defined in Peters et al. [13]. Equation (9) can be conveniently organized in the form of

$$\dot{\boldsymbol{\lambda}}=\mathbf{F}_1\ddot{\mathbf{q}}+\mathbf{F}_2\dot{\mathbf{q}}+\mathbf{F}_3\boldsymbol{\lambda} \tag{10}$$

where

$$\begin{aligned}\mathbf{F}_1&=\mathbf{E}^{-1}\left[\mathbf{c}\quad\left(\tfrac{1}{2}b-d\right)\mathbf{c}\right]\\ \mathbf{F}_2&=\mathbf{E}^{-1}\left[\mathbf{0}_{N\times 1}\quad U_0\mathbf{c}\right]\\ \mathbf{F}_3&=\mathbf{E}^{-1}\left[\mathrm{diag}\left(-\frac{U_0}{b}\right)\right]_N\end{aligned} \tag{11}$$

2.2. Aeroelastic equation of motion and state-space form

To complete the aeroelastic equation, one can substitute Eq. (7) into Eq. (3) and combine with Eq. (10), yielding

$$\begin{aligned}\bar{\mathbf{M}}\ddot{\mathbf{q}}+\bar{\mathbf{C}}\dot{\mathbf{q}}+\bar{\mathbf{K}}\mathbf{q}&=\mathbf{D}_a\boldsymbol{\lambda}+\mathbf{R}_0\\ \dot{\boldsymbol{\lambda}}&=\mathbf{F}_1\ddot{\mathbf{q}}+\mathbf{F}_2\dot{\mathbf{q}}+\mathbf{F}_3\boldsymbol{\lambda}\end{aligned} \tag{12}$$

where the aeroelastic matrices, $\bar{\mathbf{M}}$, $\bar{\mathbf{C}}$, and $\bar{\mathbf{K}}$, are obtained by grouping the structural matrices in Eq. (3) and the corresponding aerodynamic matrices in Eq. (7), i.e.,

$$\bar{\mathbf{M}}=\mathbf{M}_s-\mathbf{M}_a,\quad \bar{\mathbf{C}}=\mathbf{C}_s-\mathbf{C}_a,\quad \bar{\mathbf{K}}=\mathbf{K}_s-\mathbf{K}_a \tag{13}$$

Eventually, Eq. (12) can be written in the state-space form, leading to

$$\dot{\mathbf{x}}=\mathbf{A}\mathbf{x}+\mathbf{H} \tag{14}$$

where

$$\begin{aligned}\mathbf{x}&=\begin{Bmatrix}\mathbf{q}\\ \dot{\mathbf{q}}\\ \boldsymbol{\lambda}\end{Bmatrix},\quad \mathbf{A}=\begin{bmatrix}\mathbf{I} & \mathbf{0} & \mathbf{0}\\ \mathbf{0} & \bar{\mathbf{M}} & \mathbf{0}\\ \mathbf{0} & -\mathbf{F}_1 & \mathbf{I}\end{bmatrix}^{-1}\begin{bmatrix}\mathbf{0} & \mathbf{I} & \mathbf{0}\\ -\bar{\mathbf{K}} & -\bar{\mathbf{C}} & \mathbf{D}_a\\ \mathbf{0} & \mathbf{F}_2 & \mathbf{F}_3\end{bmatrix},\\ \mathbf{H}&=\begin{bmatrix}\mathbf{I} & \mathbf{0} & \mathbf{0}\\ \mathbf{0} & \bar{\mathbf{M}} & \mathbf{0}\\ \mathbf{0} & -\mathbf{F}_1 & \mathbf{I}\end{bmatrix}^{-1}\begin{Bmatrix}\mathbf{0}\\ \mathbf{R}_0\\ \mathbf{0}\end{Bmatrix}\end{aligned} \tag{15}$$

2.3. Proposed real-time hybrid simulation platform

As discussed in the previous section, RTHS can potentially remove the restriction of sizing and save a significant amount of operation cost, compared to conventional wind-tunnel testing. However, it requires the separation of aerodynamic simulations (performed in computers) and structural vibration experiments. Fig. 2 illustrates the RTHS of a 2-D airfoil with the data exchange between aerodynamic simulation and vibration testing. The airfoil kinematic data are measured at each time step from the vibration experiment, which are fed to the unsteady aerodynamic simulation

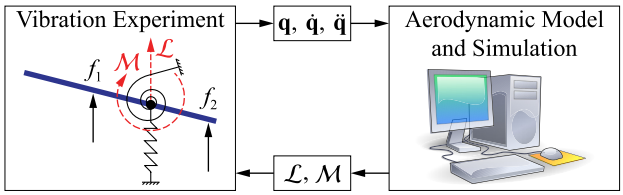

Fig. 2. Sketch of the proposed RTHS platform.

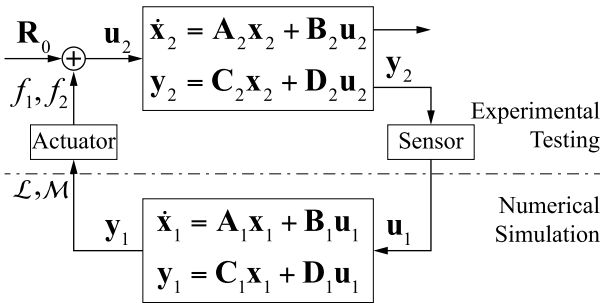

Fig. 3. RTHS with actuator and sensor function blocks.

in the computer. The simulation calculates the aerodynamic loads in real-time based upon the kinematic input, which are transformed into the actuator forces (f_1 and f_2) used to actuate the airfoil motion. The airfoil response is continuously measured and sent to the computer for the simulation, which closes the loop of RTHS for the aeroelastic system.

As a proof-of-concept study, the proposed RTHS platform is simulated numerically by modeling aerodynamic and structural dynamic subsystems individually. In the simulations, the data communication between the two subsystems is enabled to allow for the coupling. Based upon Eqs. (7) and (10), the state, output, and input variables of the aerodynamic subsystem are

$$\mathbf{x}_1 = \boldsymbol{\lambda}, \quad \mathbf{y}_1 = \left\{ -\mathcal{L} \quad \mathcal{M} \right\}^T, \quad \mathbf{u}_1 = \left\{ \mathbf{q}^T \quad \dot{\mathbf{q}}^T \quad \ddot{\mathbf{q}}^T \right\}^T \tag{16}$$

whereas the state-space equations are set up as

$$\begin{aligned} \dot{\mathbf{x}}_1 &= \mathbf{A}_1 \mathbf{x}_1 + \mathbf{B}_1 \mathbf{u}_1 \\ \mathbf{y}_1 &= \mathbf{C}_1 \mathbf{x}_1 + \mathbf{D}_1 \mathbf{u}_1 \end{aligned} \tag{17}$$

where

$$\begin{aligned} \mathbf{A}_1 &= \mathbf{F}_3, \quad \mathbf{B}_1 = \begin{bmatrix} \mathbf{0} & \mathbf{F}_2 & \mathbf{F}_1 \end{bmatrix} \\ \mathbf{C}_1 &= \mathbf{D}_a, \quad \mathbf{D}_1 = \begin{bmatrix} \mathbf{K}_a & \mathbf{C}_a & \mathbf{M}_a \end{bmatrix} \end{aligned} \tag{18}$$

On the other hand, the structural dynamic subsystem can be set up as follows, according to Eq. (3):

$$\begin{aligned} \dot{\mathbf{x}}_2 &= \mathbf{A}_2 \mathbf{x}_2 + \mathbf{B}_2 \mathbf{u}_2 \\ \mathbf{y}_2 &= \mathbf{C}_2 \mathbf{x}_2 + \mathbf{D}_2 \mathbf{u}_2 \end{aligned} \tag{19}$$

where

$$\mathbf{x}_2 = \left\{ \mathbf{q}^T \quad \dot{\mathbf{q}}^T \right\}^T, \quad \mathbf{y}_2 = \mathbf{u}_1, \quad \mathbf{u}_2 = \mathbf{y}_1 + \mathbf{R}_0 \tag{20}$$

and

$$\begin{aligned} \mathbf{A}_2 &= \begin{bmatrix} \mathbf{0} & \mathbf{I} \\ -\mathbf{M}_s^{-1}\mathbf{K}_s & -\mathbf{M}_s^{-1}\mathbf{C}_s \end{bmatrix}, \quad \mathbf{B}_2 = \begin{bmatrix} \mathbf{0} \\ \mathbf{M}_s^{-1} \end{bmatrix} \\ \mathbf{C}_2 &= \begin{bmatrix} \mathbf{I} & \mathbf{0} \\ \mathbf{0} & \mathbf{I} \\ -\mathbf{M}_s^{-1}\mathbf{K}_s & -\mathbf{M}_s^{-1}\mathbf{C}_s \end{bmatrix}, \quad \mathbf{D}_2 = \begin{bmatrix} \mathbf{0} \\ \mathbf{0} \\ \mathbf{M}_s^{-1} \end{bmatrix} \end{aligned} \tag{21}$$

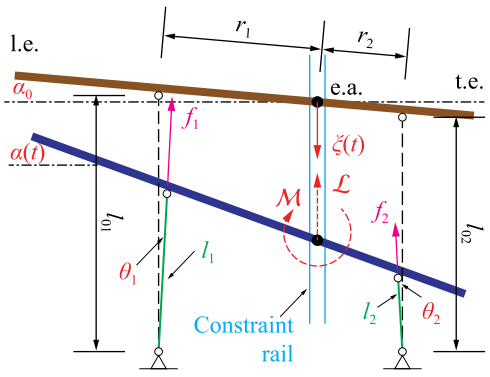

Fig. 4. Relationship between airfoil kinematics and actuator forces.

Table 1
Property of a 2-D rigid thin airfoil.

Quantity	Value
Semichord, b	0.5 m
Midchord in front of e.a., d	−0.25 m
Initial pitching angle, α_0	2.0°
Mass per unit span, m	40.0 kg m^{-1}
Structural imbalance, S_α	10.0 kg
Mass moment of inertia, I_α	5.833 kg m
Linear spring constant, K_ξ	8.0×10^3 N m^{-2}
Torsional spring constant, K_α	2.0×10^3 N
Air density, ρ	1.225 kg m^{-3}

From Eqs. (16) and (20), it can be seen that although the structural dynamic and aerodynamic subsystems are modeled separately, they are still coupled. Fig. 3 highlights the individual state-space models of structural dynamics and aerodynamics, as well as the coupling between them.

A function block of actuation is shown in Fig. 3, which takes the calculated aerodynamic loads ($\mathcal{L}$ and $\mathcal{M}$) as the input, and outputs the actuator forces (f_1 and f_2) applied on the airfoil. The actuator forces can be determined by the airfoil kinematics and the lengths of the actuators themselves. The initial actuator lengths are l_{01} and l_{02}, respectively, when $\alpha = \alpha_0$ and $\xi = 0$ (see Fig. 4). One can preset the actuators such that they both initially align in the vertical direction. The orientations of the actuator forces vary with the airfoil kinematics. At any time, the actuator forces must satisfy the following relationship to provide the equivalence of aerodynamic loads:

$$\begin{Bmatrix} f_1 \\ f_2 \end{Bmatrix} = \begin{bmatrix} \cos\theta_1 & \cos\theta_2 \\ r_1\cos(\alpha-\theta_1) & -r_2\cos(\alpha+\theta_2) \end{bmatrix}^{-1} \begin{Bmatrix} \mathcal{L}s \\ \mathcal{M}s \end{Bmatrix} \tag{22}$$

where s is the airfoil's span, usually assumed to be unity. The actuator orientations are θ_1 and θ_2, respectively. The instantaneous actuator lengths must also satisfy the geometrical compatibility condition, i.e.,

$$\begin{aligned} &[r_1(\cos\alpha_0 - \cos\alpha)]^2 + [(l_{01} - r_1\sin\alpha_0) - (\xi - r_1\sin\alpha)]^2 \\ &\quad = (l_{01} + \Delta l_1)^2 \\ &[r_2(\cos\alpha_0 - \cos\alpha)]^2 + [(l_{02} + r_2\sin\alpha_0) - (\xi + r_2\sin\alpha)]^2 \\ &\quad = (l_{02} + \Delta l_2)^2 \end{aligned} \tag{23}$$

where Δl_1 and Δl_2 are the instantaneous actuator length changes with respect to their initial values. $l_1 = l_{01} + \Delta l_1$ and $l_2 = l_{02} + \Delta l_2$ are the instantaneous actuator lengths. Based upon Eq. (23), one can derive the implicit functions of the airfoil's plunging and pitching with variables Δl_1 and Δl_2, represented by

$$\begin{aligned}\xi &= \xi(\Delta l_1, \Delta l_2)\\ \alpha &= \alpha(\Delta l_1, \Delta l_2)\end{aligned} \tag{24}$$

In RTHS, one needs to measure the actuator lengths Δl_1 and Δl_2, which in turn determine the airfoil's current plunging and pitching values. These values can be used to calculate the orientations of the actuator forces, given by

$$\begin{aligned}\sin\theta_1 &= \frac{r_1\cos\alpha_0 - r_1\cos\alpha}{l_{01}+\Delta l_1}\\ \cos\theta_1 &= \frac{(l_{01} - r_1\sin\alpha_0) - (\xi - r_1\sin\alpha)}{l_{01}+\Delta l_1}\\ \sin\theta_2 &= \frac{r_2\cos\alpha_0 - r_2\cos\alpha}{l_{02}+\Delta l_2}\\ \cos\theta_2 &= \frac{(l_{02} + r_2\sin\alpha_0) - (\xi + r_2\sin\alpha)}{l_{02}+\Delta l_2}\end{aligned} \tag{25}$$

which eventually allows to calculate the magnitudes of the actuator forces using Eq. (22).

Finally, Fig. 3 also shows a sensing block, which measures the structural responses ($\mathbf{y}_2$) of the airfoil and sends to the aerodynamic subsystem. Ideally, the input and output signals of both actuators and sensors should be equivalent. However, practical issues caused by actuators and sensors and their impacts on the proposed RTHS platform will be discussed in this paper.

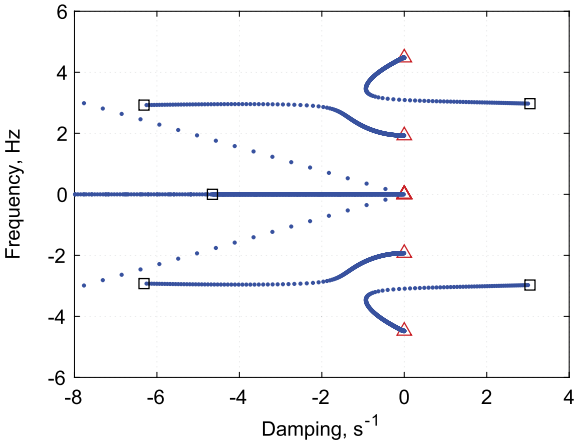

Fig. 5. Root loci of 2-D airfoil, with U_0 from 0 m s^{-1} (triangle) to 40 m s^{-1} (square).

3. Numerical studies and discussions

In this section, several numerical studies are performed to demonstrate and verify the concept of the proposed RTHS plat-

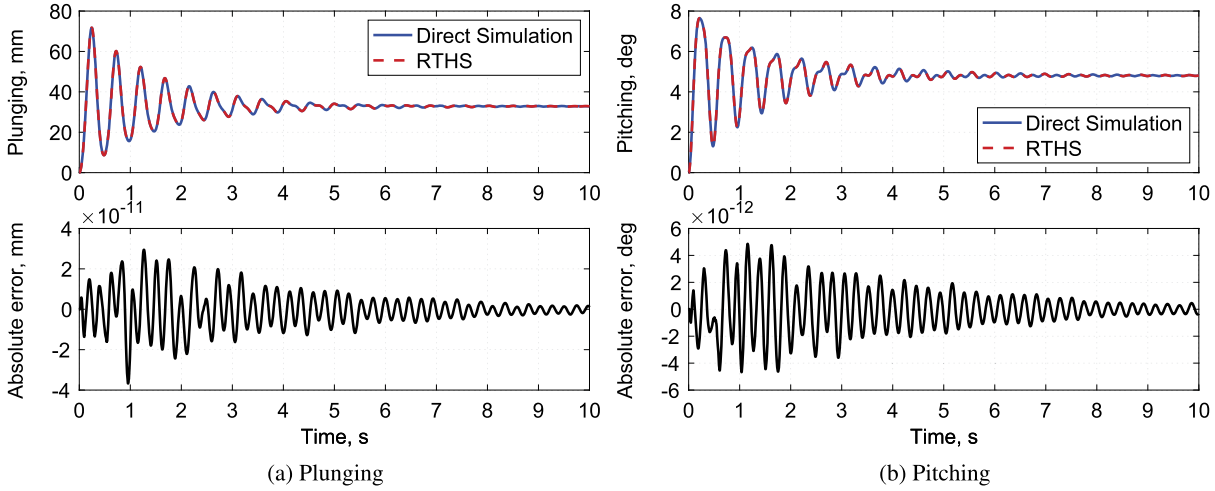

(a) Plunging (b) Pitching

Fig. 6. Comparison of airfoil responses between direct simulation and RTHS ($U_0 = 20$ m s^{-1}).

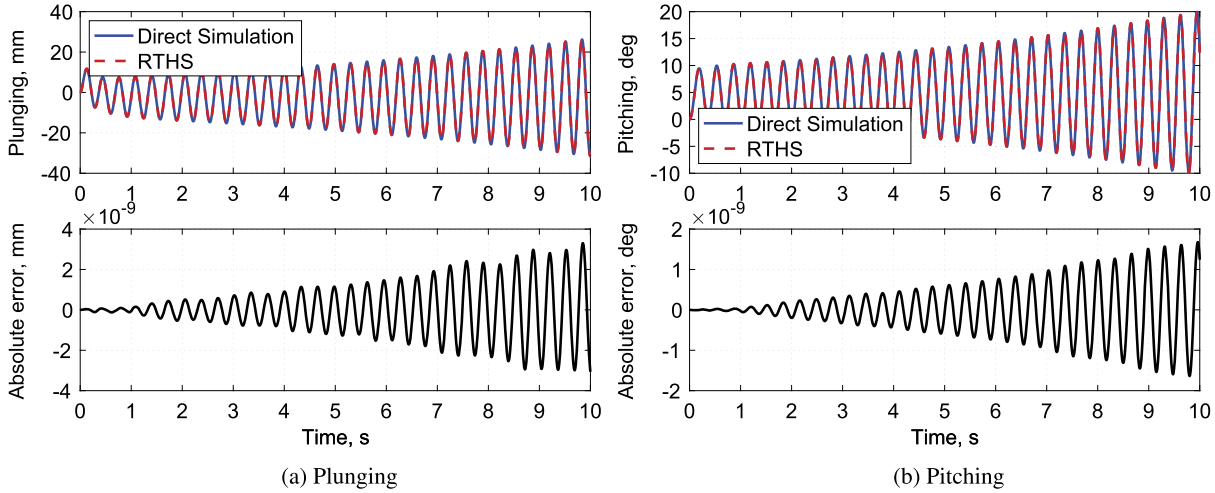

(a) Plunging (b) Pitching

Fig. 7. Comparison of airfoil responses between direct simulation and RTHS (post-flutter). (For interpretation of the colors in the figure(s), the reader is referred to the web version of this article.)

form. All studies are carried out with a 2-D thin airfoil (refer to Fig. 1), whose properties are listed in Table 1. Note that the structural damping C_ξ and C_α are both set as zero for simplicity. The aeroelastic stability characteristic of the airfoil can be conveniently identified by solving the eigenvalue problem of the system matrix **A** in Eq. (14). A sequence of **A** matrices can be formed in a range of free-stream velocity U_0. The airfoil's flutter boundary is found when a root locus crosses the imaginary axis in Fig. 5, which is $U_f = 35.59\ \mathrm{m\,s^{-1}}$. Normally, the transient aeroelastic response of the airfoil can be obtained by directly integrating Eq. (12) or (14).

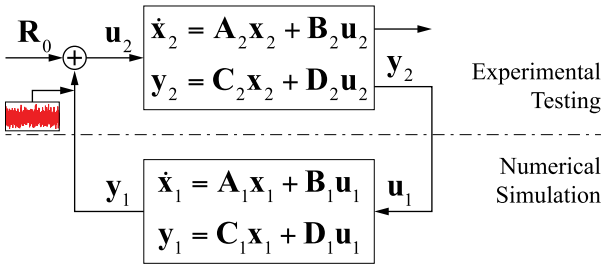

Fig. 8. RTHS with process noise.

3.1. Ideal real-time hybrid simulations

In this case, the free-stream velocity U_0 is set as 20 $\mathrm{m\,s^{-1}}$, which is below the flutter boundary. The airfoil is brought to a stationary initial condition ($\xi(0) = 0$ and $\alpha(0) = 0$), and its aeroelastic response can be solved by the direct numerical integration of the equation of motion. For an actual RTHS study, one needs to conduct the structural dynamic test physically in the lab, while exchanging data with the computational simulation of the aerodynamics in real time. In this paper, as a proof-of-concept study, the physical experiment is replicated by a numerical system, resulting in two numerical subsystems coupled together. Ideally, the transient aeroelastic response obtained from this approach is identical to the one obtained from the direct integration method. For the case demonstrated in Fig. 6, the free-stream velocity (20 $\mathrm{m\,s^{-1}}$) is less than the flutter boundary, and the transient response of the airfoil dies out due to the existing positive aerodynamic damping, and converges to the steady-state values (32.85 mm and 4.81°, respectively). This behavior is accurately captured by both simulations (with the time step of 1×10^{-3} s). More importantly, the results of the direct simulation and RTHS are almost on top of each other, evidenced by the small numerical errors shown in the plots, where the RMS (root mean square) er-

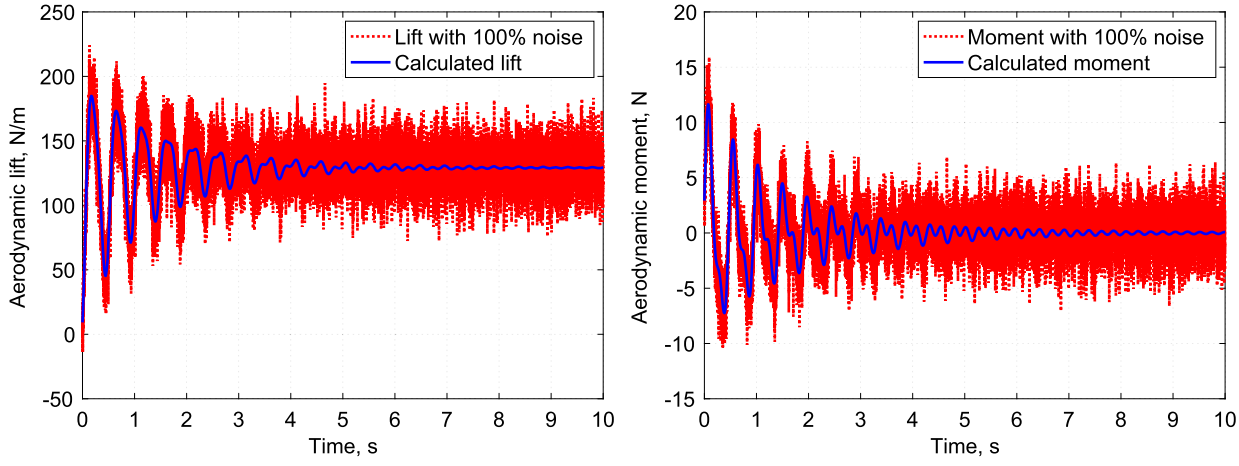

(a) Aerodynamic lift (b) Aerodynamic moment

Fig. 9. Commanded aerodynamic loads with 100% process noise.

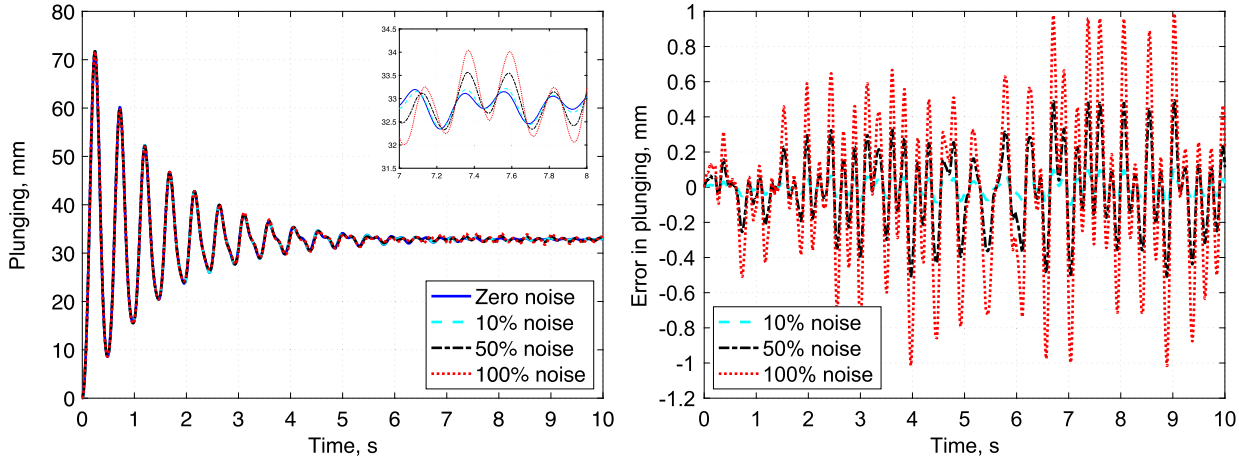

(a) Response (b) Time-wise error

Fig. 10. Impact of process noise on airfoil plunging in RTHS.

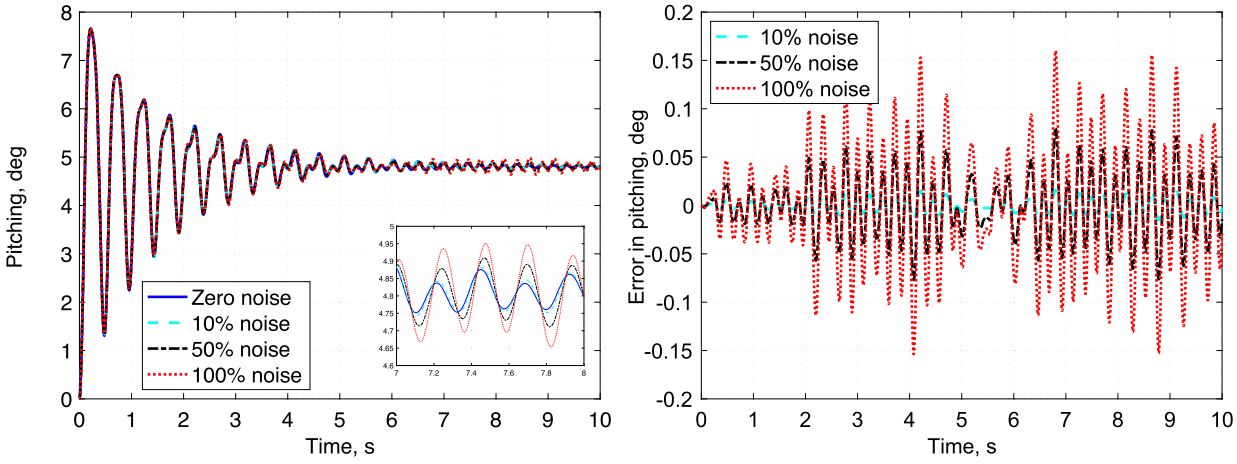

(a) Response (b) Time-wise error

Fig. 11. Impact of process noise on airfoil pitching in RTHS.

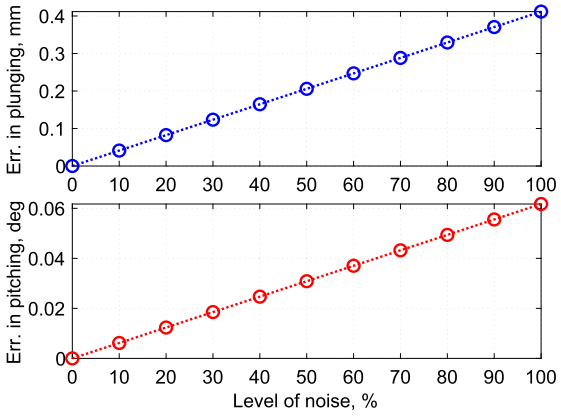

Fig. 12. RMS errors in responses with different levels of process noise.

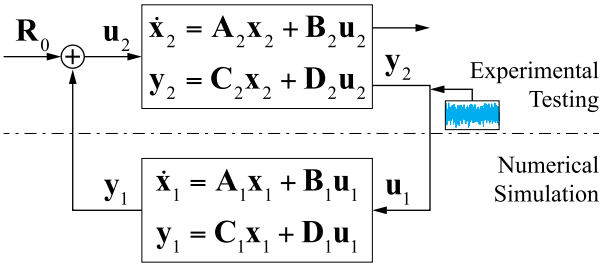

Fig. 13. RTHS with measurement noise.

rors of the plunging and pitching motions are 8.56×10^{-12} mm and 1.53×10^{-12} deg, respectively. Another comparison is performed with the free-stream velocity U_0 being 35.68 m s^{-1}, which is 0.25% above the predicted flutter boundary. As expected, the unstable aeroelastic behavior is observed from the transient simulations (Fig. 7). The results from the direct simulation and RTHS also agree well, with RMS errors of the plunging and pitching motions being 1.19×10^{-9} mm and 6.08×10^{-9} deg, respectively. From these comparisons, one can conclude that the RTHS successfully captures the same aeroelastic behavior as the direct numerical simulation does, provided that the airfoil kinematics ($\mathbf{q}$, $\dot{\mathbf{q}}$, and $\ddot{\mathbf{q}}$) can be accurately measured and the simulated aerodynamic loads are appropriately applied to excite the airfoil at each time.

3.2. Real-time hybrid simulations with process noise

In practice, RTHS cannot be conducted in such an ideal way described in the previous section. The required aerodynamic loads ($\mathcal{L}$ and $\mathcal{M}$), calculated from the numerical simulation, are applied on the airfoil through the commanded actuator forces (f_1 and f_2). The difference between the required and commanded loads should be minimized by a properly designed actuator control algorithm, which requires a thorough understanding of the coupled dynamic behavior between the actuators and the structural dynamic subsystem (the airfoil in this case). In this paper, such difference is represented by a process noise and delay effect applied on top of the calculated aerodynamic loads. This section focuses on the process noise effect, and the delay is studied in a later section (Sec. 3.4). In this section, the loads contaminated with process noise are applied to the airfoil in the experiment (see Fig. 8). By doing so, one can explore the impact of the difference between the required and commanded aerodynamic loads on the proposed RTHS, without the real actuator model and control algorithm. This treatment is believed to be sufficient in this conceptual study. The reference loads used in this study are extracted from the ideal RTHS discussed in Sec. 3.1. A Gaussian distributed random noise vector is applied to the calculated aerodynamic loads, where the noise level is set by scaling its standard deviation with respect to that of the loads in the ideal simulation. This study considers noise levels for both process and measurement (Sec. 3.3) up to 100%, which covers a broader range of noises than those considered in a recent RTHS study by Wu and Song [15]. Fig. 9 highlights the calculated aerodynamic loads and the commanded loads with noise.

Figs. 10 and 11 illustrate the transient responses of the airfoil in the RTHS with different levels of process noise. The corresponding time-wise errors are obtained by comparing to the ideal RTHS. From the figures, it seems that the system is insensitive to the noise level studied in this case. However, the process noise does cause additional airfoil vibrations, while the ideal RTHS would settle down. Fig. 12 compares the RMS errors in the airfoil's aeroelastic responses resulted from different levels of process noise. This chart helps to determine the maximum allowed difference between the calculated aerodynamic loads and the commanded loads by the actuators in the actual RTHS.

3.3. Real-time hybrid simulations with measurement noise

Sensor system may introduce measurement noise into the RTHS platform (see Fig. 3). The impact of measurement noise of the air-

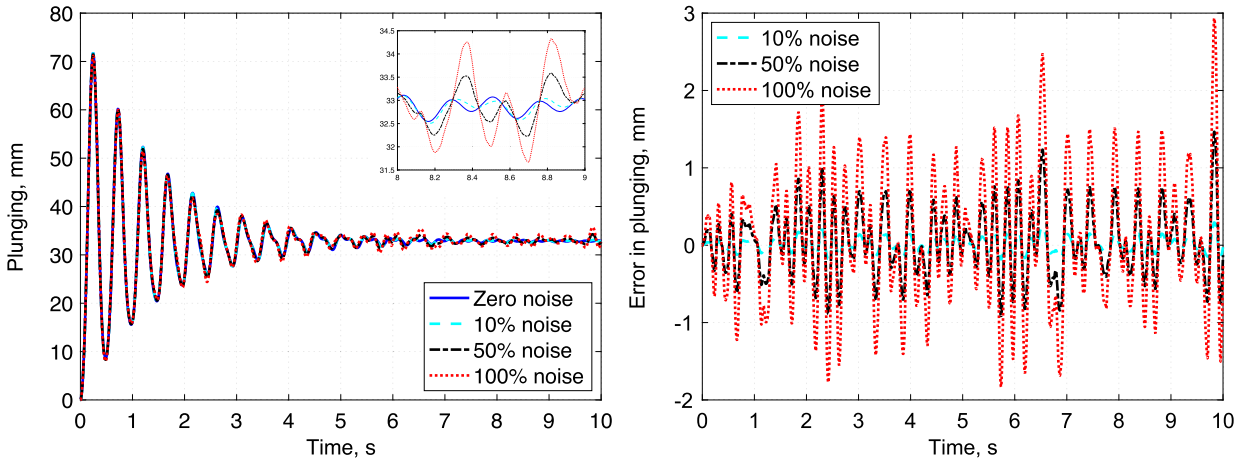

(a) Response (b) Time-wise error

Fig. 14. Impact of measurement noise on airfoil plunging in RTHS.

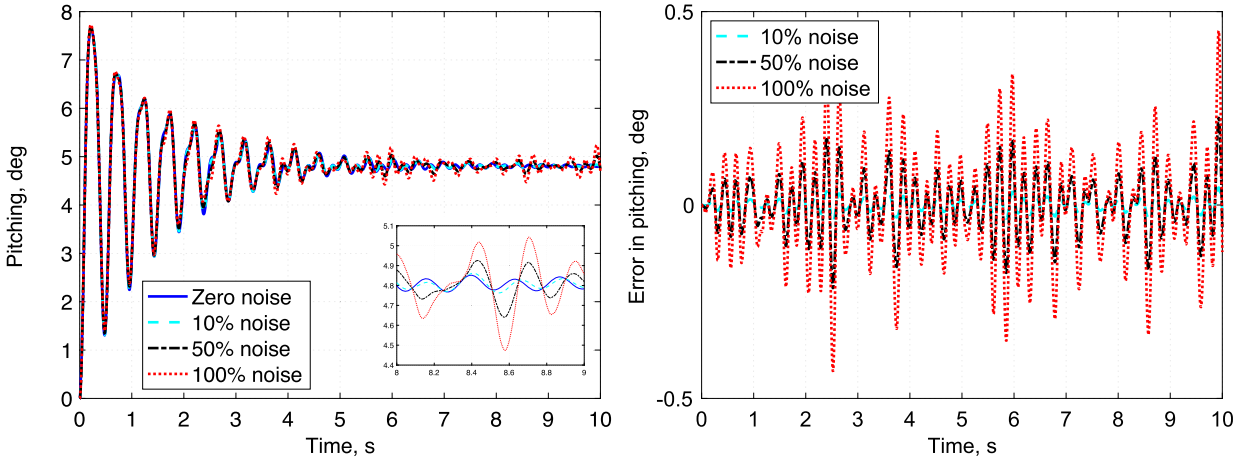

(a) Response (b) Time-wise error

Fig. 15. Impact of measurement noise on airfoil pitching in RTHS.

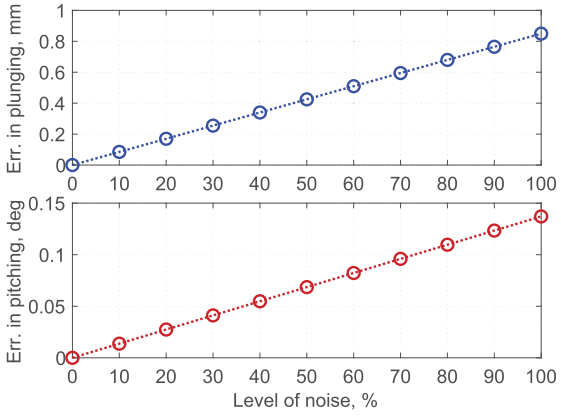

Fig. 16. RMS errors in responses with different levels of measurement noise.

foil kinematics is considered in this study. The Gaussian distributed noise is applied on the output of the structural dynamics system (**q** and its derivatives, see Fig. 13), where the level of the measurement noise is selected by scaling its standard deviation with respect to that of the airfoil responses in the ideal RTHS. Similar to the previous study, different levels of measurement noise are compared to examine their impact on the accuracy of the RTHS. Figs. 14 and 15 compare the aeroelastic behavior of the airfoil under different levels of measurement noise. The RMS errors of the airfoil behavior are plotted in Fig. 16. The impact of the measurement noise can be observed, which has a similar linear trend, as shown in Fig. 12. Note that the current study (including Sec. 3.2) only demonstrate the concept of RTHS and the aeroelastic behaviors impacted by noises. In future studies, one should calibrate the real noise level based on the properties of actuators and sensors used in RTHS.

3.4. Real-time hybrid simulations with actuator delay

Another practical consideration for RTHS is about the delay in actuation. The error caused by this latency may accumulate and eventually lead to the failure of RTHS [16]. With this regard, several numerical tests are performed to explore the impact of actuator delay on the accuracy of RTHS, with the block diagram shown in Fig. 17. In these studies, different lengths of delay are selected when the calculated aerodynamic loads are fed to the actuation, which are $2dt = 0.002$ s, $10dt = 0.01$ s, and $20dt = 0.02$ s, respectively. These delay values are higher than the

delays reported in previous RTHS studies [17,18]. The resulting airfoil plunging motions from the RTHS are then compared in Fig. 18. From Fig. 18a, it can be seen that a small amount of actuator delay (i.e., 0.002 s) does not significantly impact the airfoil's response, while a long delay may cause significant overshoots in peak values of the response. Fig. 18b compares the time-wise errors with the delays, where the error caused by the delay of twenty time steps is already comparable to the magnitude of the plunging motion. Such delays have a similar impact on the airfoil's pitching motion, as shown in Fig. 19. Fig. 20 provides a complete comparison of the RMS errors in the airfoil's aeroelastic response resulted from different actuator delays. This chart helps to determine the maximum allowed delay to maintain the required accuracy in RTHS.

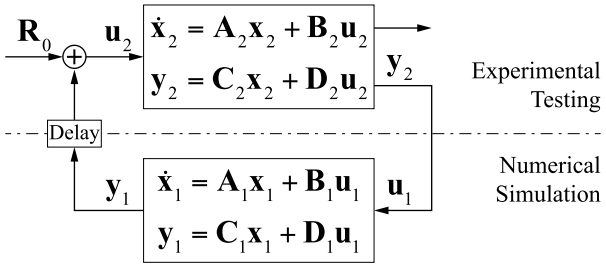

Fig. 17. RTHS with actuator delay.

3.5. Real-time hybrid simulations with both noise and delay

Finally, in the interest of discovering their combined impact, process and measurement noise, as well as actuator delay, are considered in the simulated RTHS (see Fig. 21). For simplicity, it can be assumed that the levels of process and measurement noises are identical. The relative RMS errors of the airfoil's aeroelastic response in the RTHS are plotted in Fig. 22, in which the data are normalized by the corresponding RMS transient response in the ideal RTHS (i.e., zero noises and delay, see Fig. 6). While Fig. 22 can be used to estimate the impact of noise and delays on the accuracy of RTHS, Fig. 23 provides an overall picture of the relative RMS error distributions of the airfoil's aeroelastic responses with different levels of noise and lengths of delay in the RTHS, where the two types of noises vary independently. The maximum relative RMS error of all these cases is 10.91% for plunging and 7.78% for pitching. From both Figs. 22 and 23, it is evident that in the range studied herein, the accuracy of RTHS is more sen-

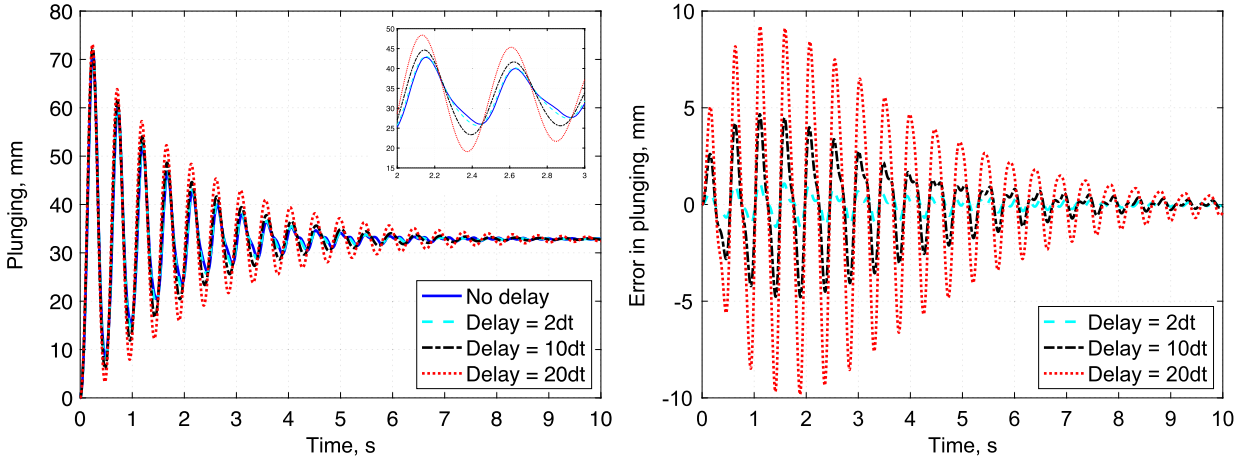

(a) Response (b) Time-wise error

Fig. 18. Impact of actuator delay on airfoil plunging in RTHS.

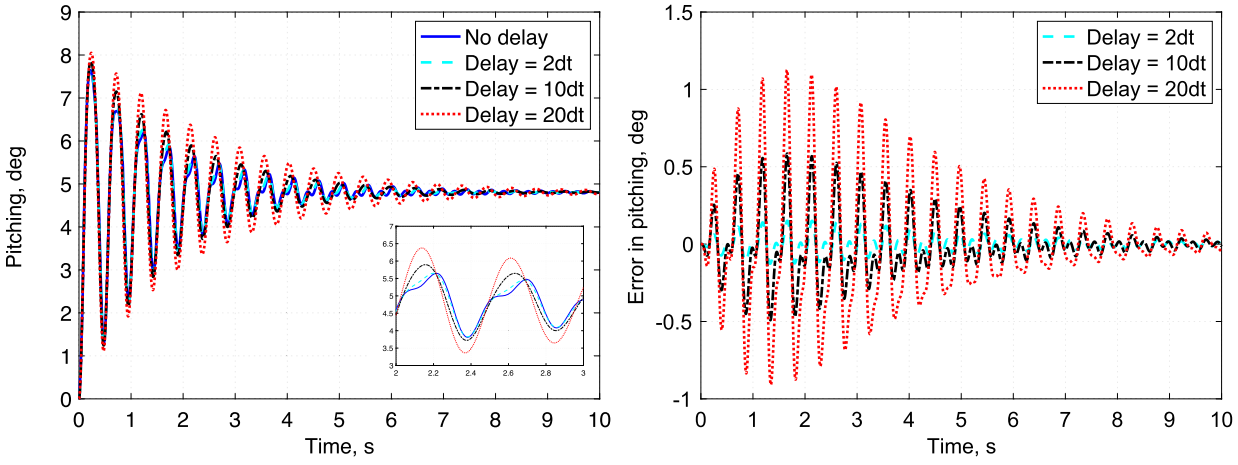

(a) Response (b) Time-wise error

Fig. 19. Impact of actuator delay on airfoil pitching in RTHS.

sitive to the length of actuator delay. For the convenience to visualize the results, Figs. 24 to 26 are generated to highlight the RMS errors under different lengths of actuator delays, where the data are collected from Fig. 23. It is of interest to discover how the two types of noise impact the simulation's accuracy with different lengths of delay. For example, when the delay is small (Fig. 24), the error increases as the level of process noise increases; but when the delay is large (Figs. 25 and 26), that trend shifts from an increasing one to decreasing. From this study, it can be seen that the airfoil's aeroelastic response predicted by the RTHS is sufficiently accurate, as long as both the noise and delay are bounded in a limited range. Based upon Figs. 23 and 25, if a maximum of 5% relative RMS error is allowed in the RTHS to maintain the required accuracy, the actuator delay cannot be greater than 10 time steps, and the measurement noise should be less than 60%.

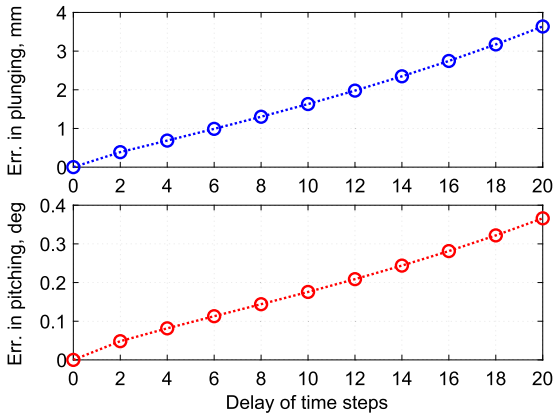

Fig. 20. RMS errors of aeroelastic responses with different lengths of delay.

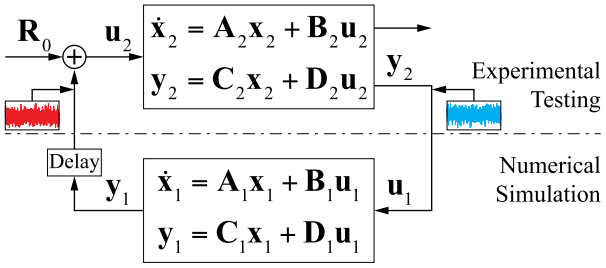

Fig. 21. RTHS with process and measurement noises, plus actuator delay.

4. Conclusion

In this paper, the concept of a proposed RTHS platform for flexible wings was presented, with a typical 2-D airfoil. Structural dynamics and aerodynamics of flexible wings are inherently coupled together, leading to their aeroelastic response. In the proposed RTHS, the aerodynamic loads on the airfoil were predicted by a proper 2-D aerodynamic formulation, while the airfoil vibration was tested in an experiment.

As a proof-of-concept study, individual state-space models were built to represent the structural dynamics and aerodynamics subsystems, and two-way data communication was set up to ensure the proper coupling between the subsystems. In the ideal situation, the proposed RTHS can accurately capture the transient aeroelastic behavior of the airfoil, including the aeroelastic instability. In practice, both actuator and sensor are used in RTHS as interfacing elements, and they introduce noises and delay into the proposed RTHS platform. By the parametric study performed in this paper, the effects of the process and measurement noises, as well as actuator delay, on the accuracy of the proposed RTHS have also been studied. It shows that the proposed RTHS can accurately capture the aerodynamic response of the airfoil, as long as the levels of the noises and delay are within a bounded range in the case of this study.

The results obtained in this study not only demonstrate the feasibility of the proposed RTHS in accurately capturing the aerodynamic behavior of the 2D airfoil but also offer insights and confidence on the robustness of the proposed RTHS under possible detrimental effects due to noises and delays. It is also worth noting that the RTHS platform proposed herein is generally applicable with properly selected aerodynamic models. Although it is not the focus of this study, where the airfoil's aerodynamic behavior is considered linear, the selection of aerodynamic models for wing members and full vehicles with different planforms and flow conditions needs to be adequately considered in the proposed RTHS platform. In future study, the authors will further consider the appropriate selection of various aerodynamic formulations and experimental implementations on the proposed RTHS platform.

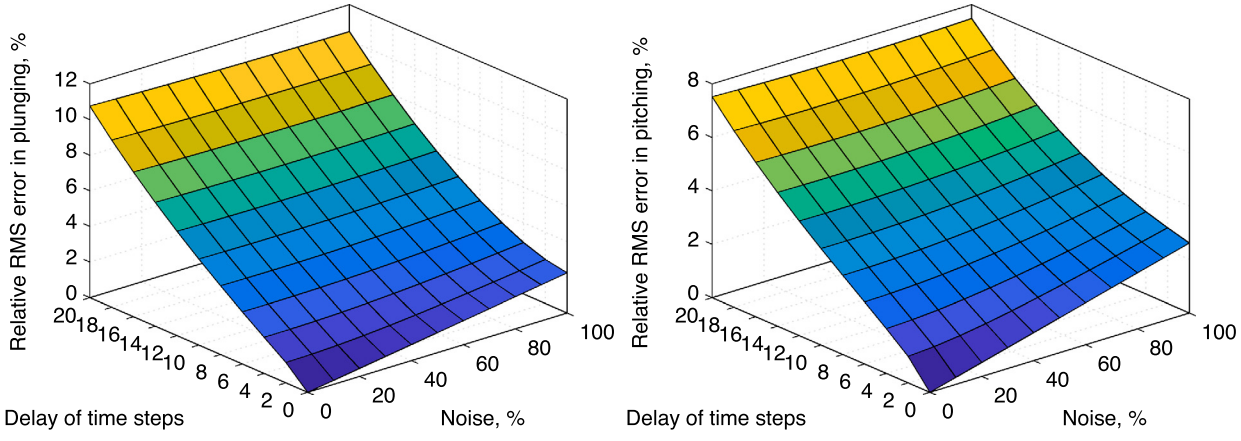

(a) Plunging (b) Pitching

Fig. 22. Relative RMS errors with different noise levels and delays in RTHS.

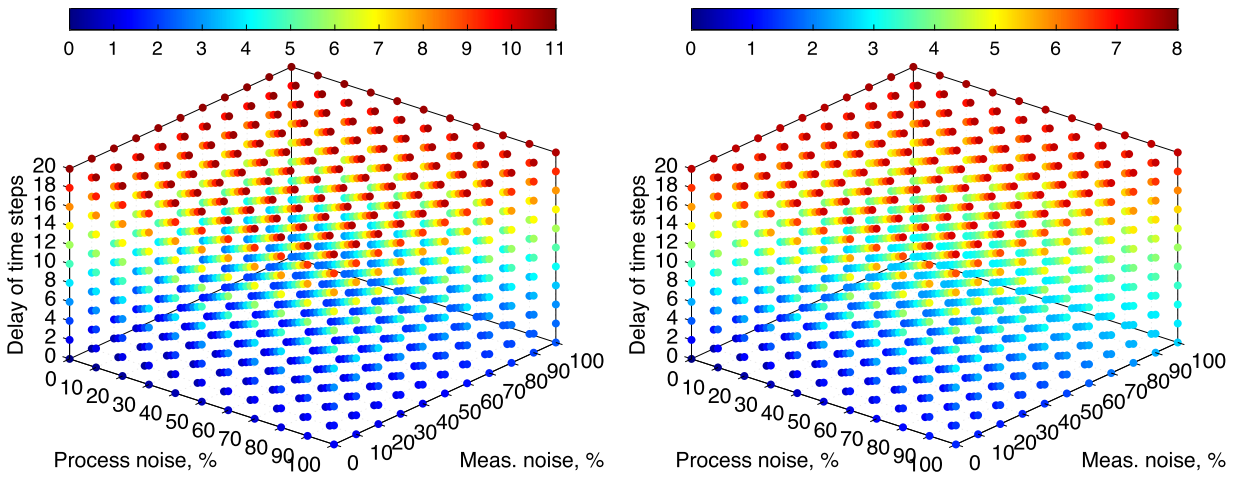

(a) Relative RMS error in plunging, %

(b) Relative RMS error in pitching, %

Fig. 23. Relative RMS errors of aeroelastic responses with different levels of noise and lengths of delay.

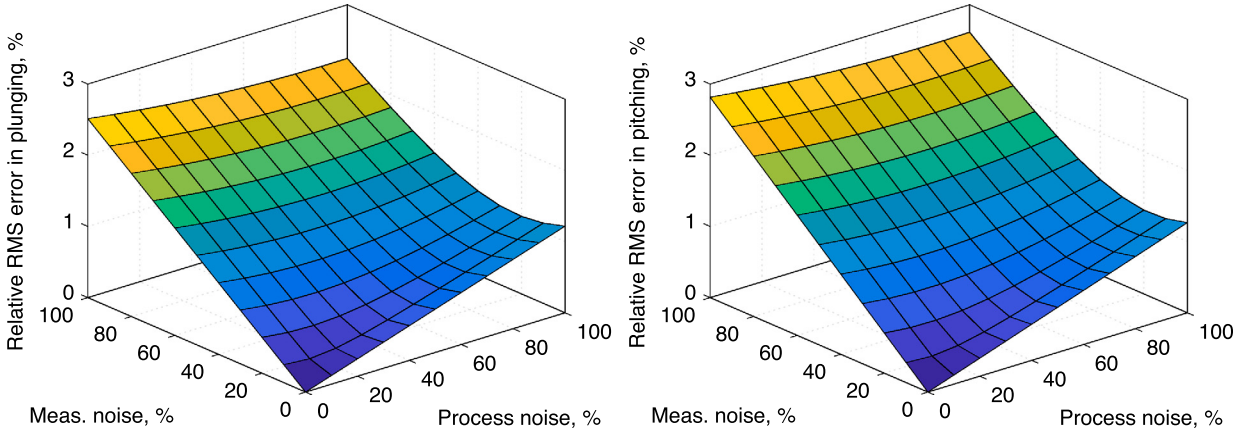

(a) Plunging

(b) Pitching

Fig. 24. Relative RMS errors with zero delay in RTHS.

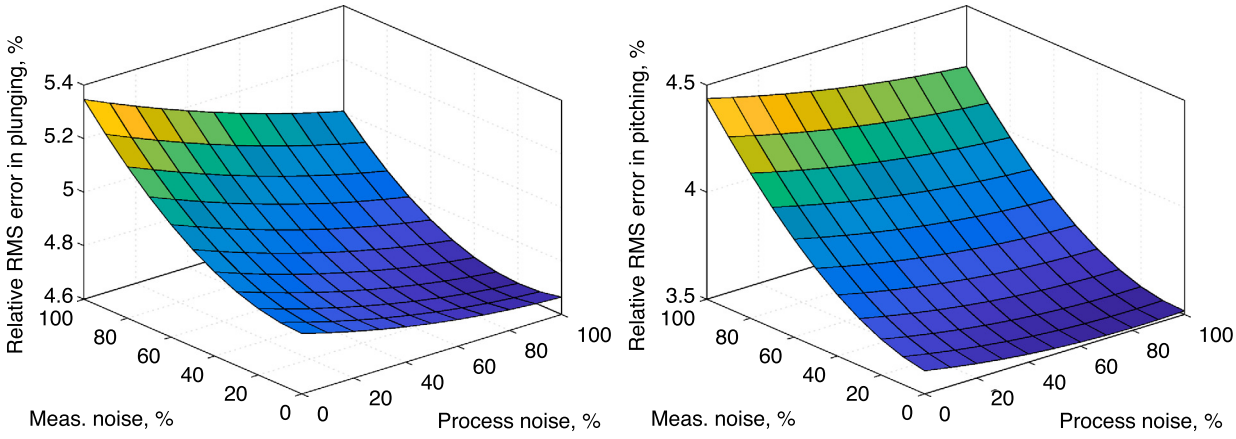

(a) Plunging

(b) Pitching

Fig. 25. Relative RMS errors with delay of 10 steps in RTHS.

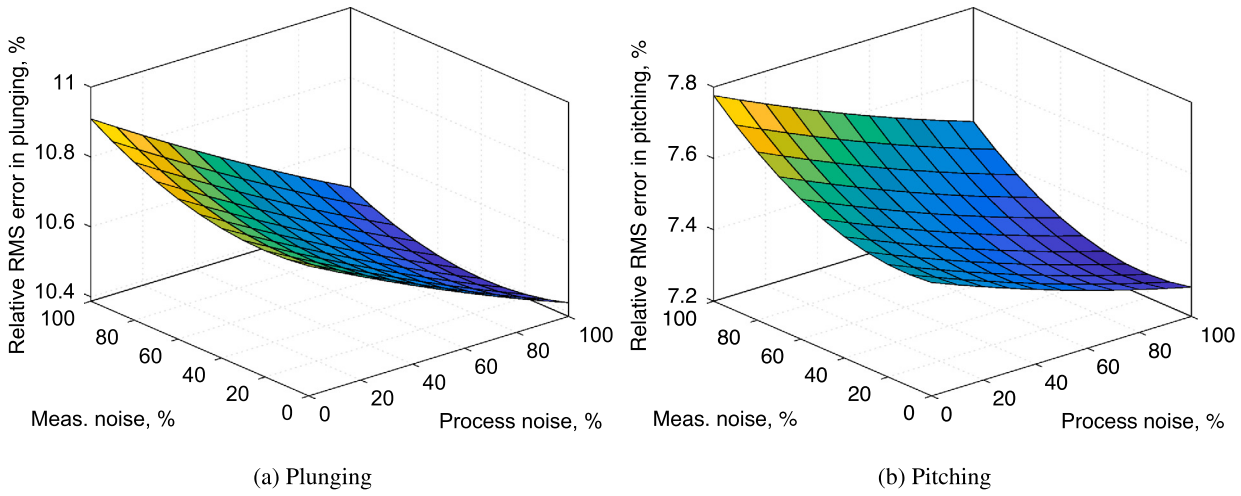

(a) Plunging (b) Pitching

Fig. 26. Relative RMS errors with delay of 20 steps in RTHS.

Declaration of competing interest

There is no competing interest.

References

[1] Q. Wei, J. Fang, X. Fan, S. Wei, Hybrid simulation system study of sins/cns integrated navigation, IEEE Aerosp. Electron. Syst. Mag. 23 (2) (2008) 17–24, https://doi.org/10.1109/MAES.2008.4460727.

[2] L. Waszniowski, Z. Hanzálek, J. Doubrava, Aircraft control system validation via hardware-in-the loop simulation, J. Aircr. 48 (4) (2011) 1466–1468, https://doi.org/10.2514/1.C031229.

[3] F. Boria, B. Stanford, S. Bowman, P. Ifju, Evolutionary optimization of a morphing wing with wind-tunnel hardware in the loop, AIAA J. 47 (2) (2009) 399–409, https://doi.org/10.2514/1.38941.

[4] T.H. Bradley, B.A. Moffitt, D.N. Mavris, T.F. Fuller, D.E. Parekh, Hardware-in-the-loop testing of a fuel cell aircraft powerplant, J. Propuls. Power 25 (6) (2009) 1336–1344, https://doi.org/10.2514/1.40805.

[5] G. Strub, S. Theodoulis, V. Gassmann, S. Dobre, M. Basset, Pitch axis control for a guided projectile in a wind tunnel hardware-in-the-loop setup, J. Spacecr. Rockets 52 (6) (2015) 1614–1626, https://doi.org/10.2514/1.A33330.

[6] R. Zappulla II, J. Virgili-Llop, C. Zagaris, H. Park, M. Romano, Dynamic air-bearing hardware-in-the-loop testbed to experimentally evaluate autonomous spacecraft proximity maneuvers, J. Spacecr. Rockets 54 (4) (2017) 825–839, https://doi.org/10.2514/1.A33769.

[7] M. Fritz, S. Winter, J. Freund, S. Pflueger, O. Zeile, J. Eickhoff, H.-P. Roeser, Hardware-in-the-loop environment for verification of a small satellite's on-board software, Aerosp. Sci. Technol. 47 (2015) 388–395, https://doi.org/10.1016/j.ast.2015.09.020.

[8] M.I. Wallace, D.J. Wagg, S.A. Neild, P. Bunniss, N.A.J. Lieven, A.J. Crewe, Testing coupled rotor blade-lag damper vibration using real-time dynamic substructuring, J. Sound Vib. 307 (3–5) (2007) 737–754, https://doi.org/10.1016/j.jsv.2007.07.004.

[9] S.A. Mahin, P.B. Shing, Pseudodynamic method for seismic testing, J. Struct. Eng. 111 (7) (1985) 1482–1503, https://doi.org/10.1061/(ASCE)0733-9445(1985)111:7(1482).

[10] M. Nakashima, H. Kato, E. Takaoka, Development of real-time pseudo dynamic testing, Earthq. Eng. Struct. Dyn. 21 (1) (1992) 79–92, https://doi.org/10.1002/eqe.4290210106.

[11] P.B. Shing, O.S. Bursi, M.T. Vannan, Pseudodynamic tests of a concentrically braced frame using substructuring techniques, J. Constr. Steel Res. 29 (1–3) (1994) 121–148, https://doi.org/10.1016/0143-974X(94)90059-0.

[12] D.A. Peters, M.J. Johnson, Finite-state airloads for deformable airfoils on fixed and rotating wings, in: P.P. Friedmann, J.C.I. Chang (Eds.), Symposium on Aeroelasticity and Fluid/Structure Interaction, in: ASME Winter Annual Meeting, vol. AD-44, American Society of Mechanical Engineers, New York, NY, 1994, pp. 1–28.

[13] D.A. Peters, S. Karunamoorthy, W.-M. Cao, Finite state induced flow models part i: Two-dimensional thin airfoil, J. Aircr. 32 (2) (1995) 313–322, https://doi.org/10.2514/3.46718.

[14] D.A. Peters, C.-J. He, Finite state induced flow models part ii: Three-dimensional rotor disk, J. Aircr. 32 (2) (1995) 323–333, https://doi.org/10.2514/3.46719.

[15] T. Wu, W. Song, Real-time aerodynamics hybrid simulation: Wind-induced effects on a reduced-scale building equipped with full-scale dampers, J. Wind Eng. Ind. Aerodyn. 190 (2019) 1–9, https://doi.org/10.1016/j.jweia.2019.04.005.

[16] A. Maghareh, S.J. Dyke, A. Prakash, G.B. Bunting, Establishing a predictive performance indicator for real-time hybrid simulation, Earthq. Eng. Struct. Dyn. 43 (2014) 2299–2318, https://doi.org/10.1002/eqe.2448.

[17] T. Horiuchi, M. Inoue, T. Konno, Y. Namita, Real-time hybrid experimental system with actuator delay compensation and its application to a piping system with energy absorber, Earthq. Eng. Struct. Dyn. 28 (10) (1999) 1121–1141, https://doi.org/10.1002/(SICI)1096-9845(199910)28:10<1121::AID-EQE858>3.0.CO;2-O.

[18] A.P. Darby, A. Blakeborough, M.S. Williams, Improved control algorithm for real-time substructure testing, Earthq. Eng. Struct. Dyn. 30 (3) (2001) 431–448, https://doi.org/10.1002/eqe.18.